

# Measurements of stress fields near a grain boundary: Exploring blocked arrays of dislocations in 3D



Y. Guo<sup>a,\*</sup>, D.M. Collins<sup>a</sup>, E. Tarleton<sup>a</sup>, F. Hofmann<sup>b</sup>, J. Tischler<sup>c</sup>, W. Liu<sup>c</sup>, R. Xu<sup>c</sup>, A.J. Wilkinson<sup>a</sup>, T.B. Britton<sup>d</sup>

<sup>a</sup> Department of Materials, University of Oxford, Parks Road, Oxford OX1 3PH, UK

<sup>b</sup> Department of Engineering Science, University of Oxford, Parks Road, OX1 3PJ, UK

<sup>c</sup> Advanced Photon Source, Argonne National Laboratory, Argonne, IL 60439, USA

<sup>d</sup> Department of Materials, Royal School of Mines, Imperial College London, London SW7 2AZ, UK

## ARTICLE INFO

### Article history:

Received 28 April 2015

Revised 22 May 2015

Accepted 25 May 2015

Available online 24 June 2015

### Keywords:

DAXM

HR-EBSD

Slip band

Grain boundary

Hall–Petch coefficient

## ABSTRACT

The interaction between dislocation pile-ups and grain boundaries gives rise to heterogeneous stress distributions when a structural metal is subjected to mechanical loading. Such stress heterogeneity leads to preferential sites for damage nucleation and therefore is intrinsically linked to the strength and ductility of polycrystalline metals. To date the majority of conclusions have been drawn from 2D experimental investigations at the sample surface, allowing only incomplete observations. Our purpose here is to significantly advance the understanding of such problems by providing quantitative measurements of the effects of dislocation pile up and grain boundary interactions in 3D. This is accomplished through the application of differential aperture X-ray Laue micro-diffraction (DAXM) and high angular resolution electron backscatter diffraction (HR-EBSD) techniques. Our analysis demonstrates a similar strain characterization capability between DAXM and HR-EBSD and the variation of stress intensity in 3D reveals that different parts of the same grain boundary may have different strengths in resisting slip transfer, likely due to the local grain boundary curvature.

© 2015 Acta Materialia Inc. Published by Elsevier Ltd. This is an open access article under the CC BY license (<http://creativecommons.org/licenses/by/4.0/>).

## 1. Introduction

Structural metals and alloys are used in a diverse range of applications, including energy, transport and the built environment. Improving the performance of these metals, typically through increased specific strength, ensures that these materials continue to meet the environmental and mechanical demands of their chosen application and exploitation in new markets. For example, in transport a reduction in weight improves fuel consumption reducing cost and limiting the environmental impact through decreased exhaust emissions.

In practice, improved properties arise from increased microstructure control and understanding of the role of specific microstructural features, such as grain boundaries, and how defects, such as dislocations, interact with these features to control strength, ductility and failure. Furthermore, grain boundaries necessarily impart heterogeneous mechanical responses at the local scale which can be critical in damage nucleation processes. If we can understand these processes, we can exploit processing

strategies and resources to engineer microstructures with specific interface types, providing a step-change in properties governed by grain boundary interactions [1].

The role of grain boundaries in strengthening materials is well known and leads to the empirical Hall–Petch relationship [2,3], as well as other important chemical and mechanical properties [4–11]. The ability to relate properties to grain boundary character [12–16] was principally driven through new characterization techniques, and in particular electron backscatter diffraction (EBSD). However, the subsurface boundary plane orientation has rarely been taken into account, primarily as it is difficult to measure, requiring cross sectioning or 3D characterization. It has been shown that the 3D structure of the boundaries is important, as a change of grain boundary plane orientation while keeping all other properties fixed results in a dramatic change in material properties [8,17]. In general EBSD measures four parameters of each grain boundary, three for crystal misorientation and one that describes the trace of the grain boundary plane on sample surface. The final parameter, which describes sub-surface inclination requires sectioning to measure for individual boundaries [18], and can be accessed for many boundaries using statistical treatments [19].

\* Corresponding author.

Alternative measurements using X-rays [20,21] can also be employed.

Apart from the 5 geometry parameters, the surface roughness of grain boundaries [7,10,22] has also been shown to be important for a variety of material properties such as creep and grain boundary sliding [23,24], and yielding of polycrystalline metals [25]. In practice, it is likely that a full representation of grain boundary characteristics requires more than 5 parameters, where the grain boundary topography and even local segregation of alloying elements could also play a significant role.

The differences in characteristics of grain boundaries are reflected not only by their collective effect on bulk properties but also by their individual interactions with slip bands. A slip transfer criterion was proposed by Shen et al. [26,27] and was further developed by Lee et al. [28–30] (known as the LRB criteria) to account for the relative orientations of the grain boundary plane and the slip systems on either side of the boundary. The criterion was proven to be effective from both modeling [31–33] and experimental [34,35] works but with an emphasis on the importance of detailed grain boundary structures and the precise location of the dislocation/grain boundary intersection on the predictability of a set of rules governing slip band/grain boundary interactions.

Dislocations can interact with a grain boundary in three ways: direct transmission; leaving a residual Burgers vector at the grain boundary [33]; or be absorbed forming grain boundary dislocations, which could either spread along the grain boundary plane or become pinned at some points [36–38]; a dislocation pile-up leading to stress ahead of the boundary, and subsequent activation of slip in the neighbor grain that can transmit dislocations toward the boundary and eliminate dislocations within the pile-up. In practice these processes are affected by the structure of the grain boundary [37] and necessarily result in different stress states in the neighboring grains [34].

Over the last decade, the ability and need to characterize microstructural features in 3D has emerged [21,39,40], as some 3D investigations reported that conclusions based on 2D studies were insufficient [41–43] and in places incorrect. In this current research, we study the interactions between dislocation pile-up and grain boundary using differential aperture X-ray Laue micro-diffraction technique (DAXM, 3D) and provide the first results on the 3D nature of such interactions. Our results in 3D are compared with a previous 2D investigation. The 3D results outline an added layer of complexity involving the curvature of the boundary sub-surface.

## 2. Materials and experimental procedures

Grade 1 commercial purity ( $\geq 99.1\%$ ) titanium was supplied by Timet (Birmingham, UK). This alloy is a single phase alpha titanium with a hexagonal close packed structure and minimal alloying additions. Tensile specimens with dimensions specified in Fig. 1 were machined using electron discharged machining (EDM) and heat treated at 830 °C for 24 h followed by slow cooling to minimize residual stress and to obtain large grain sizes ( $\sim 300 \mu\text{m}$ ). This sample was ground using SiC paper and polished using repetitive etching and colloidal silica polishing, until high quality EBSD patterns were observed. The sample was deformed quasi-statically at a strain rate of  $1 \mu\text{m/s}$  to 1% macroscopic tensile plastic strain using Shimadzu AGS-10 precision universal tester coupled with 'TRViewX' digital video extensometer. The average strain level of the gauges section was monitored using in situ digital image correlation.

The dominant deformation mechanism at this strain level and rate was confirmed to be dislocation slip using both optical microscopy and scanning electron microscopy. After mechanical deformation a number of high resolution EBSD maps ( $10 \mu\text{m} \times 25 \mu\text{m}$ ,

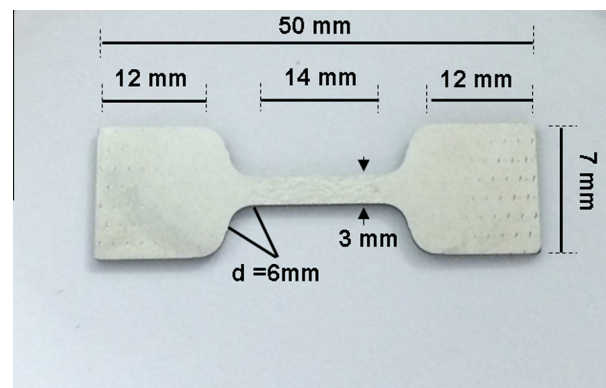


Fig. 1. Tensile specimen design. Thickness of the samples were cut to 2 mm but the actual thickness of the final test piece varies depending on the polishing process. The thickness of the specimen used for this investigation was  $\sim 1.5 \text{ mm}$ .

with  $0.2 \mu\text{m}$  step size) were recorded of slip band and grain boundary interactions, using a JOEL JSM 6500 scanning electron microscopy. At each electron beam position the diffraction patterns were saved as  $1000 \times 1000$  pixel TIFF images with 12-bit depth using OIM Data Collection V5. Residual stress distributions associated with these interactions were calculated by cross-correlating the saved diffraction patterns following the method documented in [44,45]. One example of a blocked slip band that HR-EBSD had shown to lead to a significant stress concentration was investigated using differential aperture micro-beam Laue X-ray diffraction microscopy (DAXM), performed at beam line 34-ID-E at the Advanced Photon Source (APS).

In the DAXM experiment, a polychromatic X-ray beam was focused using two non-dispersive Kirkpatrick–Baez focusing mirrors producing a beam with a Lorentzian profile with a full width half maximum of  $\sim 0.5 \mu\text{m}$ . Diffraction patterns were recorded on a Perkin-Elmer flat panel detector ( $409.6 \times 409.6 \text{ mm}^2$ ,  $2.048 \times 2.048$  pixels, amorphous Si, CsI scintillator, 16-bit dynamic range corresponding to 65,536 counts) mounted in  $90^\circ$  reflection geometry 510.3 mm above the sample. The experimental geometry was calibrated using measurements of a thin stress free silicon sample ( $< 5 \mu\text{m}$  thickness). Overlapping Laue patterns, corresponding to different depths in the sample, were measured at each beam position on the sample. The depths of origin of different scattered contributions were determined by wire scanning, allowing the reconstruction of depth-resolved Laue patterns [20]. Key to this process is the accurate positioning, alignment and scanning of the wire with respect to the sample surface. In this experiment, this was performed using careful calibration of the detector alignment to ensure that depth profiling produces reproducible results within the Si membrane reference sample.

The titanium sample was positioned in the X-ray beam using a low depth of field optical microscope, confining the inclined ( $45^\circ$  with respect to horizontal plane) surface plane of the specimen to a specific region where the X-ray beam strikes. A region of interest was selected based upon the prior HR-EBSD investigation [34] and marked using focused ion beam trenches and Pt depositions with an aim of using X-ray fluorescence (XRF) to determine the location. The sample surface was scanned at  $1 \mu\text{m}$  intervals. At each interrogation point the wire was swept across the sample. Ray-tracing reconstruction of Laue patterns from individual voxel was performed with LaueGo software using the wire-scan data. Reconstructions were performed to a depth of  $190 \mu\text{m}$  into the sample with a  $1 \mu\text{m}$  depth spacing. This was repeated to generate a series of slices that form a volume map of the size  $23 \mu\text{m} \times 31 \mu\text{m} \times 190 \mu\text{m}$ , as is shown in Fig. 2, with  $1 \mu\text{m}^3$  voxel size.

For each voxel, pattern indexing, strain refinement, and lattice rotation calculation were performed using LaueGo software at 34-ID-E. As the volume map contained only two grains, the solutions for two example Laue patterns of the two crystal orientations were verified manually. The lengths of the  $\langle c \rangle$  and  $\langle a \rangle$  axis for Ti were calibrated using a monochromatic beam and a  $c/a$  ratio of 1.588 was measured. Orientations and reference frames were directly compared between EBSD measurements and the Laue diffraction analysis and were found to be consistent. In addition to extracting the strain and rotation tensors, a reliability factor based upon the number of spots used in the indexing is reported. This was used to filter out erroneous ‘ghost points’ from above the sample surface, observed due to the nature of decoding the overlapping diffraction patterns with the back-subtraction algorithm from the DAXM analysis procedure. Data were exported into Matlab for further computation and 3D volumes were rendered in Avizo.

### 3. Results

For slip band and grain boundary interactions, theoretical work by Eshelby, Frank, and Nabarro [46] provided an excellent model (referred to as EFN model) to quantify the level of stress concentration caused by a blocked slip band. When the number of dislocations in the pile up is high the model predicted that the stress in the neighboring grain as a result of the shearing on the slip plane decreases in an approximately ‘one over square root distance’ fashion directly ahead of the pile up away from the grain boundary [34,46,47]. The stress intensity factor,  $K$ , can be extracted by fitting this stress profile with experimental data.

For HR-EBSD, elastic strain variations relative to the strain status at the reference points within each grain were calculated following methods documented in prior work [44,45]. These elastic strain tensor variations were then used to calculate stress variations using single crystal elastic constants and anisotropic Hooke’s law [34,47]. To assess the stress induced in the neighboring grain as a result of the shearing in the deformed grain associated with the blocked slip plane, the measured stress is rotated to provide the shear stress associated with the active slip system (prismatic plane) defined by  $X_1^i$ ,  $X_2^i$ , and  $X_3^i$  in Fig. 3.

The stress profile ahead of the blocked slip band (Fig. 3) was fitted with the expression:  $\sigma_{31}^r = A + K/\sqrt{X+B}$  [47], to extract the  $K$  factor. Here  $\sigma_{31}^r$  is the resolved shear stress by the dislocation pile-up in the neighboring grain and  $X$  is the distance along the line profile away from the grain boundary. The constants  $A$  and  $B$  are introduced to allow for uncertainty of reference stress state ( $A$ ) and grain boundary position ( $B$ ) respectively.

The same grain boundary as shown in Fig. 3 was investigated using DAXM and deviatoric strain was obtained from this experiment. The use of white beam prevents measurement of the hydrostatic strain [48]. For each voxel the stress tensor was extracted using anisotropic Hooke’s law and the crystal orientation with image slices parallel to  $X_{\text{beam}}$  and  $Z_{\text{beam}}$  (Fig. 2) plane. The appropriate coordinate transfer from the beam-line frame of reference into the slip plane was performed, after which all 31 slices of images were stacked together to reconstruct the original volume. The voxels with a lower magnitude of stress ( $\sim 50$  MPa) in grain 2 (Fig. 5) were made transparent to visualize the grain boundary and the stress concentration due to the blocked slip planes in the 3D volume rendering produced with Avizo and shown in Fig. 4.

For each slice of the rotated stress map, the stress profile ahead of each blocked slip band was fitted, using  $\sigma_{31}^r = A + K/\sqrt{X+B}$ , from the  $\sigma_{13}^r$  component map of the stress tensor. An example of the stress distribution ahead of the five blocked slip bands, as numbered in Fig. 4, together with the one measured using HR-EBSD is shown in Fig. 5.

Fig. 5 displays five slices of the  $\sigma_{13}^r$  stress component maps, which is the experimentally measured stress tensor component,  $\sigma_{13}$ , rotated onto the activated slip plane. The slip bands are revealed by the parallel bands of higher stress level ( $\sim 100$  MPa) in grain 1, as indicated by the arrow in Fig. 5. The dashed line on each image indicates where the accompanying stress/distance map was extracted and the solid line indicates the trace of the grain boundary on  $X_{\text{beam}}-Z_{\text{beam}}$  plane. Curve fitting to the EFN model revealed different levels of stress intensity ( $K$ ) in front of the blocked slip bands. Due to smaller step size ( $0.2 \mu\text{m}$  for HR-EBSD,  $1 \mu\text{m}$  for DAXM) the HR-EBSD method captured the stress distribution in much more detail as can be seen from the density of data points on the HR-EBSD stress/distance plot. The specific case of slip band/grain boundary interaction captured by HR-EBSD as the one shown in Fig. 3 (which is the same as the last image in Fig. 5) was not captured by DAXM due to poor indexing near free surface, therefore, direct comparison between HR-EBSD and DAXM was not possible.

### 4. Discussion

Grain boundaries play a significant role in improving grain strength in engineering materials. This is likely due to the interruption of crystal slip at the boundary and the shielding of dislocation sources due to the stress field generated by the local pile-up, thus inhibiting further slip. The ability of different grain boundaries to improve strength depends on the resistance to slip transfer at the individual boundary which can now be measured with HR-EBSD in 2D and DAXM in 3D. These techniques enable different grain boundaries to be measured and enable the growth of new rules for inclusion of grain boundary strength in models and simulations.

Investigation of dislocation band and grain boundary interaction using the combination of HR-EBSD and DAXM represents a bottom-up mesoscale understanding of local stress rises associated with these interactions which now must be captured by modeling efforts more accurately to outline the contribution of individual grain boundaries to mechanical strength and performance. This is necessarily involved, as crystal plasticity approaches may ‘smear out’ the local stress fields associated with individual dislocation pile ups. Furthermore, these observations and modeling approaches must be homogenized appropriately to capture many grains in larger component scale analyses to be used by design engineers. In particular, contributions from a similar slip system interacting with subtle variations in the grain boundary geometry show some variation in local stress intensity which is likely associated with both the number of dislocations within the pile-up as well as the local grain boundary structure. Here we have shown that the 2D measurements of the local stress state enable measurement of the stress intensity factor from the EFN model. 3D measurements of the stress intensity and grain boundary morphology significantly improve these measurements, as the effect of the local curvature of the grain boundary can be taken into account.

The feature of interest chosen for DAXM investigation was selected using high resolution electron backscatter diffraction (HR-EBSD) technique [44,45], the result of which can be found in Fig. 3. It is clear from the DAXM results in Fig. 4 that the surface map obtained with HR-EBSD (Fig. 3) represents a slice in 2D of the ‘slip band’ (i.e. plane) and grain boundary interaction in 3D. The highly localized region of high stress that is seen in 2D (Fig. 3) is extended into a ‘ribbon’ in 3D (an animation showing Fig. 4 rotating in 3D space is provided in the Supplementary data). Furthermore, different slip plane grain boundary interactions result in subtly different stress concentrations at different locations on the same slip plane.

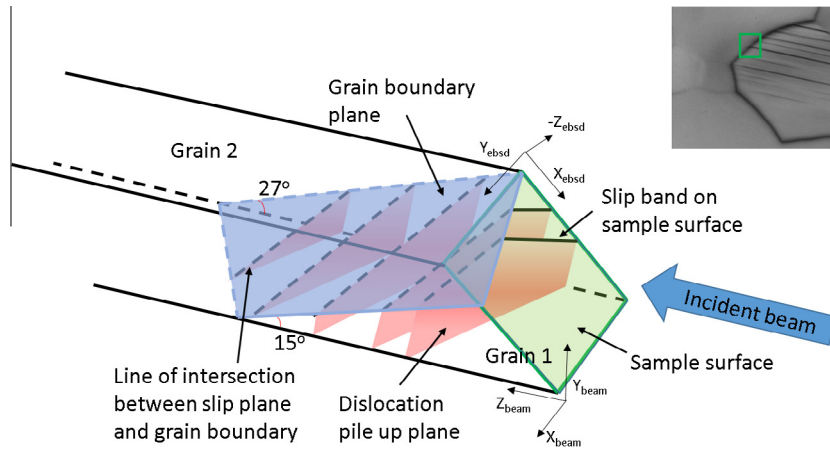


**Fig. 2.** Visualization of the probed volume. Grain boundary is approximated to be planar and colored light blue in this image. Dislocation pile up plane is colored red and the dashed lines on the blue grain boundary plane represent the line of intersection between slip plane and grain boundary. The solid line on sample surface plane (colored green) represents the slip band which is visible under optical microscopy and SEM. Coordinate systems  $X_{\text{ebdsd}}$ ,  $Y_{\text{ebdsd}}$ ,  $Z_{\text{ebdsd}}$  and  $X_{\text{beam}}$ ,  $Y_{\text{beam}}$ ,  $Z_{\text{beam}}$  indicate the special arrangement of EBSD reference system and X-ray beam reference system respectively with respect to the measured sample volume. Inserted image to the upper right corner is an optical image of the sample surface, showing this specific case of slip band/grain boundary interaction and the approximate position of the experiments (green box). (For interpretation of the references to color in this figure legend, the reader is referred to the web version of this article.)

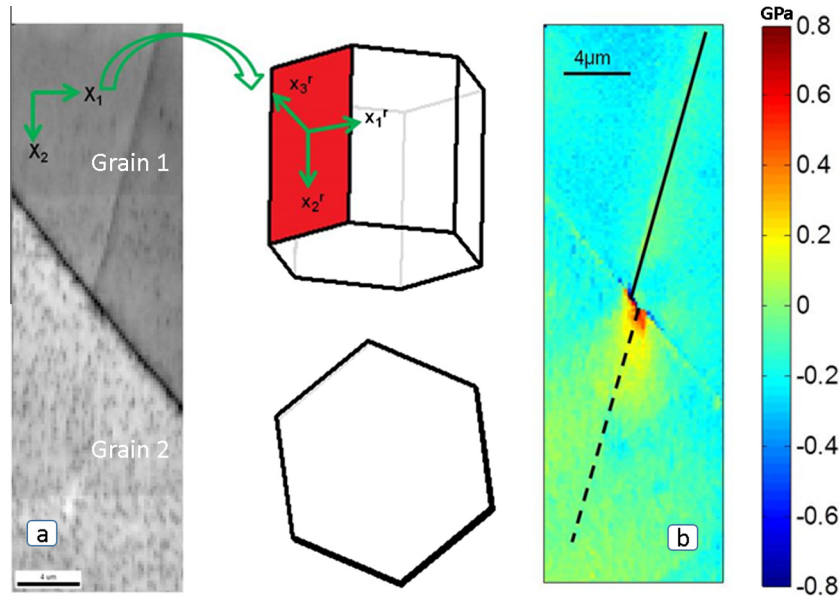


**Fig. 3.** HR-EBSD results of a blocked slip band (remade from reference [34]). (a) The EBSD image quality map revealing an impinging slip band in the upper grain and no visible slip activity in the neighboring grain. Red plane on the hexahedron in the upper middle image shows the activated prismatic slip plane.  $X_1$  and  $X_2$  are coordinates of the EBSD image while  $X_1'$ ,  $X_2'$ , and  $X_3'$  are coordinates defined by the active slip system. (b) HR-EBSD map of resolved shear stress  $\sigma_{13}$  revealing localized stress concentration in front of the slip band/grain boundary intersection, the solid line indicates the position of the incident slip band, the dashed line indicates the direction along which stress line profile was taken. (For interpretation of the references to color in this figure legend, the reader is referred to the web version of this article.)

Slip trace analysis confirmed that the slip traces (slip band) from both EBSD and DAXM measurements originated from the same slip plane. The alignment between the activated slip plane and various slip systems, including  $\langle a \rangle$  basal,  $\langle a \rangle$  pyramidal,  $\langle a \rangle$  prismatic, and  $\langle c+a \rangle$  pyramidal, were represented using an ‘ $M$  factor’ derived from the LRB slip transfer criteria [28],  $M = \frac{(\mathbf{n}_i \cdot \mathbf{b}_j)(\mathbf{b}_i \cdot \mathbf{b}_j)}{|\mathbf{b}_i||\mathbf{b}_j|}$ , where  $\mathbf{n}$  and  $\mathbf{b}$  are slip plane normal and Burgers vector respectively. The best alignment between the active prismatic slip system in grain 1 was found to be the  $\langle c+a \rangle$  pyramidal slip systems in grain 2, posing a ‘difficult to transfer’ situation and leading to a localized stress concentration. The stress field shown in Figs. 3 and 5 has been rotated from the beamline frame of reference onto the active slip plane to reveal

the stress caused by shearing of the active slip system. The rotated stress field can be quantified as a stress intensity factor,  $K$ , using the approach of Britton and Wilkinson [47] based upon the solution by Eshelby et al. [46]. The variation of  $K$  along band 1–5 (Fig. 4) and average  $K$  for each band are shown in Fig. 6(a) and (b) respectively.

Band 1 captures the stress variation from close to the free sample surface to bulk (in the absence of a suitable DAXM surface measurement) as its rightmost data point (Fig. 6(a)) is only 5  $\mu\text{m}$  away from the free surface. The measured stress intensity value at this point is  $0.18 \pm 0.01 \text{ MPa m}^{1/2}$ , about 40% lower than the average value of  $0.31 \pm 0.11 \text{ MPa m}^{1/2}$  measured for this band. Moving away from this point into the bulk of the sample (to the left of the graph), the stress intensity fluctuates around the mean



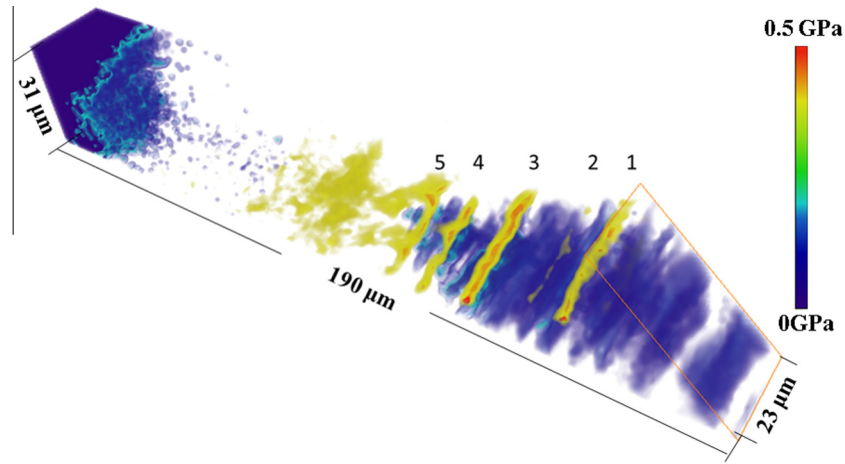


**Fig. 4.** 3D visualization of the shear stress concentration induced by the blocked slip planes. Green to light yellow colors in grain 2 (Fig. 5) represent data points with lower strain/stress magnitude. They were made transparent to bring out the remaining orange/red colors that (5 bands) reveal the stress distribution along the line of intersection between slip plane and grain boundary. (For interpretation of the references to color in this figure legend, the reader is referred to the web version of this article.)

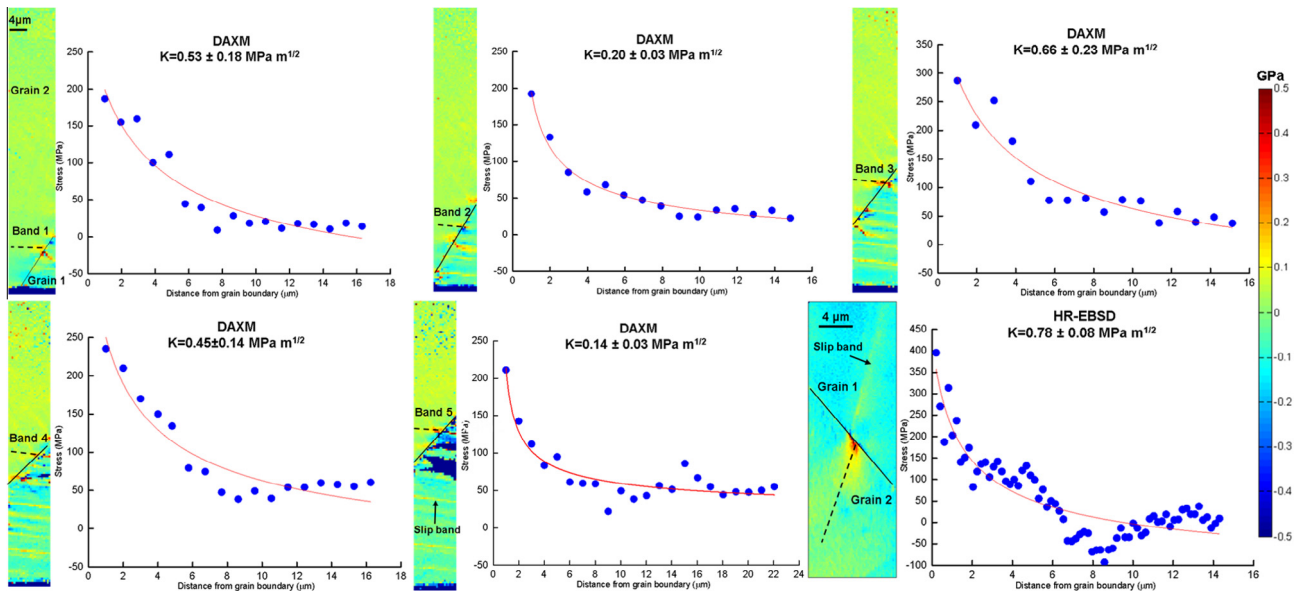


**Fig. 5.** Slices of the deviatoric residual elastic stress maps of the 3D volume taken in the  $X_{\text{beam}}-Z_{\text{beam}}$  plane (this reference frame is defined in Fig. 2). Numbering of slip bands corresponds to the numbering in Fig. 4. Line profile of the stress distribution was taken along each of the dashed line. As comparison, the stress intensity profile from the HR-EBSD measurement (Fig. 3) is also shown as the final image.

value, reflecting the local grain boundary effect, most notably the local grain boundary curvature which has been confirmed to present in various alloy systems through field ion microscopy [7,10] and more advanced high precision focused ion beam serial sectioning technique [24]. It is also possible that intrinsic grain boundary defects as well as local chemical variations could adjust the pile-up strength and these have not been measured here. These fluctuations of  $K$  are, however, of similar magnitude to the error bars associated with determining  $K$  from the stress profile. The variation of  $K$  along slip band 1 (and indeed for the other slip bands) does not suggest any strong systematic variation with depth from the free surface over length scales of several microns. Moreover, the fluctuation of stress intensity over a single line of intersection between slip plane and grain boundary (Fig. 6(a)) is within similar range with those obtained from HR-EBSD on different grain boundaries [34], this seems to suggest that for higher length scale models the slip transmission criteria can be treated as a probabilistic process.

Variations of stress intensity are seen both along the same line of intersection between slip plane and grain boundary (Fig. 6(a)) and between the different lines of intersections (Fig. 6(b)). The range of  $K$  is as high as 68% of the mean along band 1 and 67% between band 2 and band 3. This poses the question to what extent it is possible to accurately predict the site at which material damage (e.g. crack) or deformation twinning will nucleate. While it is relatively easy to identify the most damage prone site (band 3 in this case), the exact position for the most probable damage nucleation along band 3 (or any other line of intersections) is likely to be stochastic, depending on the interactions between individual dislocations and local grain boundary features. This effect is likely to lead to two scenarios which require 3D characterization, and 2D observations will be less than conclusive:

1. If damage nucleation is observed as a surface stress riser in 2D, there is a possibility that a large population of damage already exists beneath the sample surface.

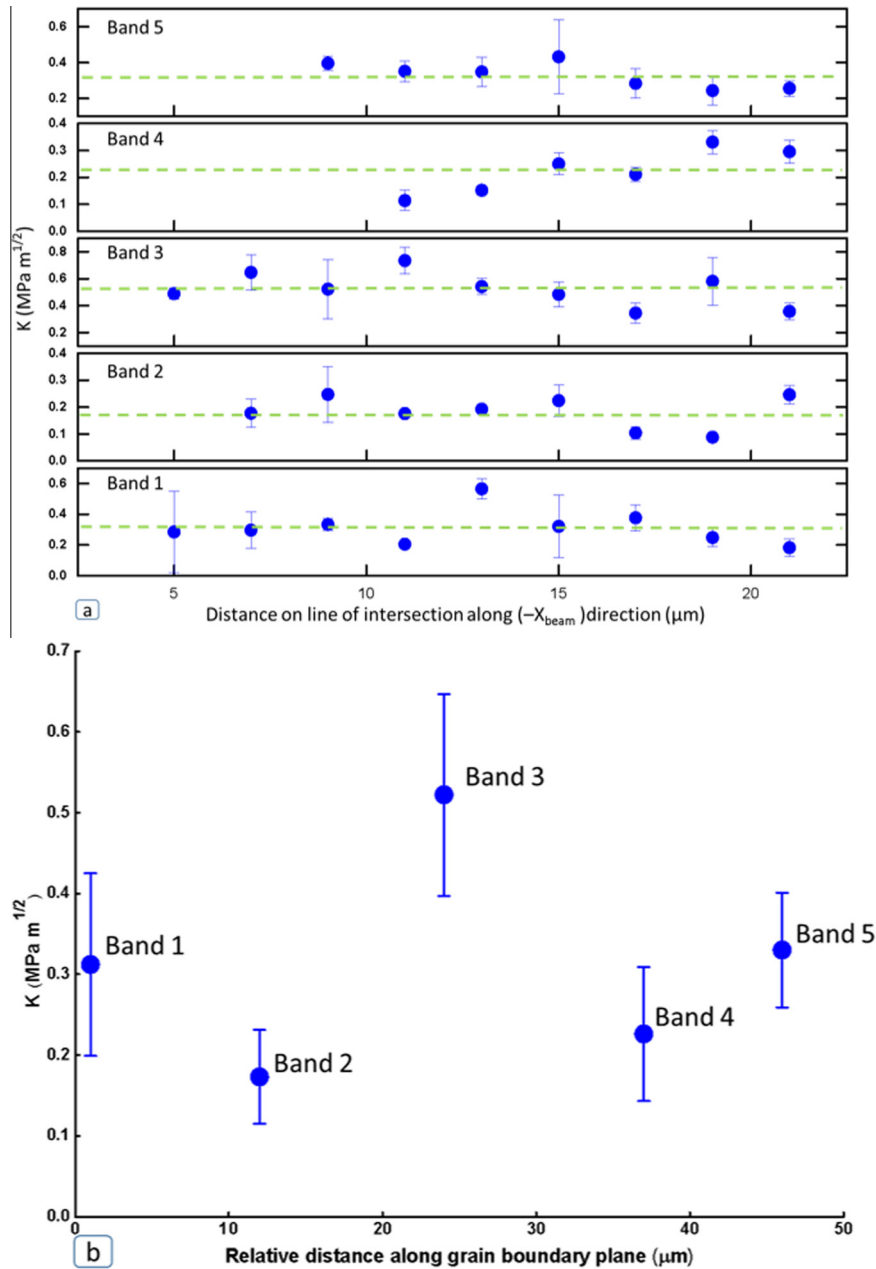


**Fig. 6.** (a) Stress intensity factor,  $K$ , variation along the line of intersection between slip plane and grain boundary. For each band, data points from left to right correspond to bottom left to top right in Fig. 4. Green dashed line indicates the average  $K$  value of each band. (b) Shows the average  $K$  value of each band plotted against approximate distance from the first band. (For interpretation of the references to color in this figure legend, the reader is referred to the web version of this article.)

## 2. Observation, or not, of damage in 2D may not be representative of damage observations in microstructural features in 3D.

Variation in the stress intensity also indicates that different parts of grain boundary have different barrier strengths to dislocation transmission (either direct or indirect) as we have previously observed no stress intensity (i.e.  $K = 0$ ) in the case of slip transfer [34].

The angle between the grain boundary plane and the bottom plane of the data volume was measured to be about  $15^\circ$  to the left and  $27^\circ$  to the right (as shown in Fig. 2), indicating the presence of grain boundary curvature. The  $M$  factor that represents local alignment of slip system across the grain boundary was calculated at both left and right side of the data volume and two approaches were used: the first one utilizing the angle between slip plane

normal as was suggested by Werner et al. [49] and the second one using the angle between the line of intersections between slip planes and the grain boundary as was suggested in the original LRB criteria [28]. The reason Werner et al. propose to use slip plane normal is that it is more experimentally accessible and is independent of grain boundary curvature, while the knowledge of the line of intersection between slip plane and grain boundary usually require either synchrotron or serial sectioning experiment. The results of the  $M$  factor calculation are documented in Table 1. It can be seen that at the measured range of grain boundary curvature, both the Werner approximation and the true LRB criteria are able to indicate which slip system in the neighboring grain have the maximum alignment factor with the incoming slip system. However, the maximum alignment appears for different variants of the same slip system, as shown in Table 1. This variation of

**Table 1**

Geometric alignment between impinging prismatic slip system and various slip systems in the neighboring grain. The alignment was quantified using the true LRB criteria (using angles between line of intersections between incident slip system and grain boundary) measured at the left and right side of the data volume (M (LRB-left) and M (LRB-right)). As a comparison, the substitutional LRB criteria (using angles between slip plane normal), as was proposed by Werner et al. [49], M (Werner), were also calculated.

	Basal			Prismatic		
	<11-20>(0001)	<-1-210>(0001)	<-2110>(0001)	<11-20>(1-100)	<-1-210>(-1010)	<-2110>(01-10)
M (Werner)	0.072	0.005	0.067	0.13	0.011	0.286
M (R-LRB-left)	0.054	0.004	0.05	0.257	0.02	0.261
M (R-LRB-right)	0.016	0.001	0.015	0.308	0.02	0.243
<a> Pyramidal						
	<11-20>(1-101)	<-1-210>(-1011)	<-2110>(01-11)	<11-20>(1-10-1)	<-1-210>(-101-1)	<-2110>(01-1-1)
M (Werner)	0.035	0.004	0.243	0.141	0.011	0.144
M (R-LRB-left)	0.078	0.016	0.102	0.235	0.012	0.133
M (R-LRB-right)	0.159	0.013	0.125	0.172	0.015	0.063
<c+a> Pyramidal						
	<11-23>(1-101)	<-1-123>(10-11)	<-1-213>(0-111)	<-12-13>(1-10-1)	<-2113>(10-1-1)	
M (Werner)	0.397	0.258	0.435	0.447	0.616	
M (LRB-left)	0.783	0.509	0.774	0.795	0.561	
M (LRB-right)	0.937	0.609	0.778	0.799	0.523	
<c+a> Pyramidal						
<2-1-13>(0-11-1)	<11-2-3>(1-101)	<-1-12-3>(10-11)	<-1-21-3>(0-111)	<-12-1-3>(1-10-1)	<-211-3>(10-1-1)	<-2-1-1-3>(0-11-1)
0.921	0.258	0.397	0.447	0.435	0.921	0.616
0.839	0.509	0.783	0.795	0.774	0.839	0.561
0.781	0.609	0.937	0.799	0.778	0.781	0.523

slip system alignment along a grain boundary plane is consistent with the previous report [35] and could be more significant when the sampled volume is bigger (when more grain boundary curvatures are captured).

The DAXM results capture the 3D nature of slip-plane grain boundary interactions and underpin our mechanical understanding of the effect of grain boundaries at blocking slip transfer between grains. This information is important as we move away from simple empirical 'Hall-Petch' approaches which have been recently critically reevaluated by Dunstan and Bush by [50], who suggest that the Hall-Petch relationship may not be most appropriate at describing the mechanical role of smaller grains on the strength of polycrystalline aggregates.

Fig. 5 compares the stress profile in front of the five blocked slip bands extracted from five slices in the  $X_{\text{beam}}$  and  $Z_{\text{beam}}$  plane of the DAXM measurement together with the one from HR-EBSD measurement (Fig. 3). It can be seen that the stress profiles captured from both techniques converge with the EFN model [46], but HR-EBSD offers more detail of the stress distribution than the DAXM technique due to better spatial resolution achievable in SEM. This difference in spatial resolution between the two techniques may affect the measured stress profiles, especially the stress distribution within the initial 2  $\mu\text{m}$  from grain boundary. The data point  $\sim 0.8 \mu\text{m}$  away from the grain boundary shows a markedly higher stress value for HR-EBSD than the DAXM measurement, which is likely due to positioning of the electron beam near a discrete dislocation toward the head of the pile-up [51] or possibly as a result of local chemical effect [52], while the DAXM measurement maybe averaged over too large a volume to capture such local effects. Moving away from the locations very close to grain boundary ( $>1 \mu\text{m}$ ), the stress field probed by HR-EBSD and DAXM has shown good accordance in both magnitude and distribution. The variation of stress intensity between different slip band/grain boundary interactions results in the difference in the fitted  $K$  value between HR-EBSD and DAXM as shown in Fig. 5.

## 5. Conclusion

Grain boundaries are very important microstructural features, improving the strength of real materials and they offer an extrinsic opportunity for materials engineers to modify materials performance through processing. In the present work, the stress field

due to slip band and grain boundary interaction was probed using DAXM and were compared with previous HR-EBSD investigation. The results demonstrate a similar strain/stress measurement capability between the two techniques. While the HR-EBSD technique provides more information in a much more local length scale, the stress field is based on a reference whose stress state is unknown. As a comparison, DAXM has a coarser spatial resolution but offers absolute stress state measurement and information in 3D.

The stress intensity was found to vary significantly along individual line of intersection between slip plane and grain boundary. Variations can also be seen between different lines of intersections along the grain boundary surface. The variations of stress intensity are likely due to local irregularities and global curvatures along grain boundary plane and indicate more than five parameters to completely describe the characteristics of grain boundary.

These discoveries allow us to conclude that it is now possible to pin point which dislocation pile up is likely to lead to material damage initiation (void, crack, etc.) by a systematical assessment of position dependent strength of a single grain boundary. However, a stochastic approach might be needed to capture in more detail the damage nucleation behavior of the most susceptible dislocation pile ups. This work points to a critical need for physically based dislocation based models that incorporate the realistic shape of the grain boundary, which may be captured by high fidelity 2D and 3D techniques or novel test strategies.

## Acknowledgments

Y.G., D.C., E.T., A.J.W. and T.B.B. would like to thank EPSRC for providing funding through the HexMat programme Grant (EP/K034332/1). This research used resources (34-ID-E) of the Advanced Photon Source, a U.S. Department of Energy (DOE) Office of Science User Facility operated for the DOE Office of Science by Argonne National Laboratory under Contract No. DE-AC02-06CH11357.

## Appendix A. Supplementary data

Supplementary data associated with this article can be found, in the online version, at <http://dx.doi.org/10.1016/j.actamat.2015.05.041>.

## References

- [1] T.R. Bieler, P. Eisenlohr, F. Roters, D. Kumar, D.E. Mason, M.A. Crimp, D. Raabe, The role of heterogeneous deformation on damage nucleation at grain boundaries in single phase metals, *Int. J. Plast.* 25 (9) (2009) 1655–1683.
- [2] E.O. Hall, The deformation and aging of mild steel, *Proc. Phys. Soc. B* 64 (1951).
- [3] N.J. Petch, Cleavage strength of polycrystals, *J. Iron Steel Inst.* (1953) 26.
- [4] P.J.E. Forsyth, R. King, G.J. Metcalfe, B. Chalmers, Grain boundaries in metals, *Nature* 158 (1946) 875–876.
- [5] T. Watanabe, P.W. Davies, Grain boundary sliding and intergranular fracture behavior of copper biocrystals, *Philos. Mag. A* 37 (5) (1977) 649–681.
- [6] T. Watanabe, An approach to grain-boundary design for strong and ductile polycrystals, *Res. Mech.* 11 (1) (1984) 47–84.
- [7] H.C. Eaton, A.C. Chou, J.C. Carter, Topographic analysis of grain boundary dislocations in cold-worked tungsten using field ion microscopy, *Phys. Status Solidi A* 72 (1982).
- [8] G.S. Rohrer, C.S. Kim, A.D. Rollet, Grain boundary planes: new dimensions in the grain boundary character distribution, *Scripta Mater.* 54 (2006) 1005–1009.
- [9] C.A. Schuh, S. Patala, J.K. Mason, Improved representation of misorientation information for grain boundary science and engineering, *Prog. Mater. Sci.* 57 (2012) 1383–1425.
- [10] H.F. Ryan, J. Suiter, Grain boundary topography in tungsten, *Philos. Mag.* 10 (106) (1964) 727–729.
- [11] S.J. Fensin, E.K. Cerreta, G.T. Gray, S.M. Valone, Why are some interfaces in materials stronger than others, *Sci. Rep.* 4 (2014) 5461.
- [12] G. Palumbo, P.J. King, K.T. Aust, U. Erb, P.C. Lichtenberger, Grain-boundary design and control for intergranular stress-corrosion resistance, *Scr. Metall. Mater.* 25 (1991).
- [13] T. Watanabe, Grain boundary engineering for high performance structural and functional materials, *J. Phys. IV* 10 (P6) (2000) 41–46.
- [14] T. Watanabe, S. Tsurekawa, Toughening of brittle materials by grain boundary engineering, *Mater. Sci. Eng. A* 387 (89) (2004) 447–455.
- [15] V. Randle, Twinning related grain boundary engineering, *Acta Mater.* 52 (14) (2004) 4067–4081.
- [16] T. Watanabe, S. Tsurekawa, The control of brittleness and development of desirable mechanical properties in polycrystalline systems by grain boundary engineering, *Acta Mater.* 47 (15–16) (1999) 4147–4185.
- [17] G.S. Rohrer, V. Randle, C.S. Kim, Y. Hu, Changes in the five-parameter grain boundary character distribution in alpha brass brought about by iterative thermomechanical processing, *Acta Mater.* 54 (2006) 4489–4502.
- [18] D.J. Rowenhorst, A. Gupta, C.R. Feng, G. Spanos, 3D crystallographic and morphological analysis of coarse martensite: combining EBSD and serial sectioning, *Scripta Mater.* 55 (1) (2006) 11–16.
- [19] G.S. Rohrer, Measuring and interpreting the structure of grain-boundary networks, *J. Am. Ceram. Soc.* 94 (3) (2011) 633–646.
- [20] B.C. Larson, W. Yang, G.E. Ice, J.D. Budai, J.Z. Tischler, Three-dimensional X-ray structural microscopy with submicrometer resolution, *Nature* 415 (2002) 887–890.
- [21] E.M. Lauridsen, R.W. Fonda, J.D. Jensen, Nondestructive approaches for 3D materials characterization, *JOM* 58 (12) (2006) 40–44.
- [22] D.G. Brandon, Structure of high angle grain boundaries, *Acta Metall.* 14 (1966).
- [23] R.D. Gifkins, A mechanism for the formation of intergranular cracks when boundary sliding occurs, *Acta Mater.* 4 (1) (1956) 98–99.
- [24] J.L.W. Carter, N. Zhou, J.M. Sosa, P.A. Shade, A.L. Pilchak, M.W. Kuper, Y. Wang, H.L. Fraser, M.D. Uchic, M.J. Mills, Characterization of strain accumulation at grain boundaries of nickel base superalloys, in: *Superalloys 2012: 12th International Symposium on Superalloys*, 2012.
- [25] J.C.M. Li, Petch relation and grain boundary sources, *Trans. Metall. Soc. AIME* 227 (1963).
- [26] Z. Shen, R.H. Wagoner, W.A.T. Clark, Dislocation pile-up and grain boundary interactions in 304 stainless steel, *Scr. Metall.* 20 (1986) 921–926.
- [27] Z. Shen, R.H. Wagoner, W.A.T. Clark, Dislocation and grain boundary interactions in metals, *Acta Metall.* 36 (1988) 3231–3242.
- [28] T.C. Lee, I.M. Robertson, H.K. Birnbaum, Prediction of slip transfer mechanisms across grain boundaries, *Scr. Metall.* 23 (1989) 799–803.
- [29] T.C. Lee, I.M. Robertson, H.K. Birnbaum, TEM in situ deformation study of the interaction of lattice dislocations with grain boundaries in metals, *Philos. Mag. A* 62 (1989) 131–153.
- [30] T.C. Lee, I.M. Robertson, H.K. Birnbaum, An in situ transmission electron microscope deformation study of the slip transfer mechanisms in metals, *Metall. Trans. A* 21A (1990) 2437–2447.
- [31] M. de Koning, R.J. Kurtz, V.V. Bulatov, C.H. Henager, R.G. Hoagland, W. Cai, M. Nomura, Modelling of dislocation-grain boundary interactions in FCC metals, *J. Nucl. Mater.* 323 (2–3) (2003) 281–289.
- [32] M.P. Dewald, W.A. Curtin, Multiscale modelling of dislocation/grain boundary interactions: III 60 degree dislocations impinging on sigma 3, sigma 9, and sigma 11 tilt boundaries in Al, *Modell. Simul. Mater. Sci. Eng.* 19 (2011).
- [33] M.P. Dewald, W.A. Curtin, Multiscale modelling of dislocation/grain-boundary interactions: I. Edge dislocations impinging on sigma11 (113) tilt boundary in Al, *Modell. Simul. Mater. Sci. Eng.* 15 (2007) S193–S215.
- [34] Y. Guo, T.B. Britton, A.J. Wilkinson, Slip band-grain boundary interactions in commercial-purity titanium, *Acta Mater.* 76 (1) (2014) 1–12.
- [35] W.A.T. Clark, R.H. Wagoner, Z.Y. Shen, T.C. Lee, I.M. Robertson, H.K. Birnbaum, On the criteria for slip transmission across interfaces in polycrystals, *Scr. Metall. Mater.* 26 (1991) 203–206.
- [36] B.J. Pestman, T.M. Dehonnsson, V. Vitek, F.W. Schapink, Interaction between lattice dislocations and grain boundaries in FCC materials, *Scr. Metall.* 23 (1989) 1431.
- [37] B.J. Pestman, T.M. Dehonnsson, V. Vitek, F.W. Schapink, Interaction between lattice dislocations and grain boundaries in FCC and ordered compounds: a computer simulation, *Philos. Mag. A* 64 (1991) 951–969.
- [38] D.J. Dingley, R.C. Pond, On the interaction of crystal dislocations with grain boundaries, *Acta Metall.* 27 (1979) 667–682.
- [39] F.P.E. Dunne, Fatigue crack nucleation: mechanistic modelling across the length scales, *Curr. Opin. Solid State Mater. Sci.* 18 (4) (2014) 170–179.
- [40] K.S. Cheong, M.J. Smillie, D.M. Knowles, Predicting fatigue crack initiation through image-based micromechanical modelling, *Acta Mater.* 55 (2007) 1757–1786.
- [41] S.E. Offerman, Grain nucleation and growth during phase transformations, *Science* 298 (2002).
- [42] S. Schmidt, S.F. Nielsen, C. Gundlach, L. Margulies, X. Huang, J.D. Jensen, Watching the growth of bulk grains during recrystallization of deformed metals, *Science* 305 (2004) 229–232.
- [43] L. Margulies, G. Winther, H.F. Poulsen, In situ measurement of grain rotation during deformation of polycrystals, *Science* 291 (2001).
- [44] A.J. Wilkinson, G. Meaden, D.J. Dingley, High-resolution elastic strain measurement from electron backscatter diffraction pattern: new level of sensitivity, *Ultramicroscopy* 106 (4–5) (2006) 307–313.
- [45] T.B. Britton, A.J. Wilkinson, High resolution electron backscatter measurements of elastic variations in the presence of large lattice rotations, *Ultramicroscopy* 114 (2012) 82–95.
- [46] J.D. Eshelby, F.C. Frank, F.R.N. Nabarro, The equilibrium of linear array of dislocations, *Philos. Mag.* 42 (1951) 351–364.
- [47] T.B. Britton, A.J. Wilkinson, Stress fields and geometrically necessary dislocation density distributions near the head of a blocked slip band, *Acta Mater.* 60 (2012) 5773–5782.
- [48] G.E. Ice, J.W.L. Pang, Tutorial on X-ray microLaue diffraction, *Mater. Charact.* 60 (2009) 1191–1201.
- [49] E. Werner, W. Prantl, Slip transfer across grain and phase boundaries, *Acta Metall. Mater.* 38 (3) (1989) 533–537.
- [50] D.J. Dunstan, A.J. Bushby, The scaling exponent in the size effect of small scale plastic deformation, *Int. J. Plast.* 40 (2013) 152–162.
- [51] D. Hull, D.J. Bacon, *Introduction to Dislocations*, Elsevier Ltd., 1965.
- [52] Q. Yu, L. Qi, T. Tsuru, R. Traylor, D. Rugg, J.W. Morris, M. Asta, D.C. Chrzan, A.M. Minor, Origin of dramatic oxygen solute strengthening effect in titanium, *Science* 347 (2015) 635–639.